Supporting Information

Phase and interface co-engineered MoP_xS_y@$NiFeP_xS_y$@NPS-C hierarchical heterostructure for sustainable oxygen evolution reaction

Xiaojun Zeng,[a,#,*] Haiqi Zhang,[a,#] Ronghai Yu,[b] Galen D. Stucky[c] and Jieshan Qiu[d,*]

[a] School of Materials Science and Engineering, Jingdezhen Ceramic University, Jingdezhen 333403, China

[b] School of Materials Science and Engineering, Beihang University, Beijing, 100191, China

[c] Department of Chemistry and Biochemistry, University of California Santa Barbara, CA 93106, United States

[d] College of Chemical Engineering, State Key Laboratory of Chemical Resource Engineering, Beijing University of Chemical Technology, Beijing, 100029, China

* Corresponding author, E-mail: zengxiaojun@jcu.edu.cn (X.J. Zeng), qiujs@mail.buct.edu.cn (J.S. Qiu)

1. Characterization

The microstructures and elemental distributions of the catalysts were observed by field emission scanning electron microscope (FESEM, SU-8010, HITACHI, Japan) and equipped with energy-dispersive X-ray spectroscopy (EDS, Oxford, Xplore). Transmission electron microscopy (TEM) images and EDS mapping were recorded on a transmission electron microscope (FEI Titan Themis 200 TEM, Bruker super-X EDS). The crystal phases of the catalysts were analyzed with X-ray diffraction (XRD, D8-Advance, Bruker, Germany). The

chemical composition was investigated by X-ray photoelectron spectroscopy (XPS, Thermo scalable 250Xi). N_2 adsorption-desorption isotherms were performed on a Micromeritics surface area analyzer (BRT, ASAP2020 M, Micromeritics, America) to evaluate the Brunauer Emmett Teller (BET) specific surface area and pore size of the catalysts.

2. Electrochemical measurements

The OER performance of the catalyst was analyzed on the CHI760E electrochemical workstation equipped with a rotating device (RRDE-3A, ALS Inc, Tokyo, Japan). The reference electrode, counter electrode, and working electrode were platinum wire, saturated silver/silver chloride electrode, and glassy carbon electrodes (3 mm in diameter), respectively. All tests were performed in 1 M KOH solution. To successfully prepare the working electrode, 4 mg of catalyst was first added to 1 mL Nafion solution (5 wt%) and sonicated for 2 h. The obtained ink was then dropped onto the glassy carbon electrode with a load of 0.2 mg cm^{-2}. Cyclic voltammetry (CV) curves were tested at a non-faradic current region with different scan rates (60, 80, 100, 120, and 140 mV s^{-1}). Linear sweep voltammetry (LSV) curves were analyzed at a scan rate of 5 mV s^{-1}. Electrochemical impedance spectrum (EIS) curves were investigated in the frequency range from 0.01 Hz to 100 kHz at 5 mV AC voltage. The measured potential versus Ag/AgCl was converted to a reversible hydrogen electrode (RHE) scale ($E_{RHE} = E_{Ag/AgCl} + 0.0591*pH + 0.197$) according to the Nernst equation.

3. Computation section

Within the framework of density functional theory (DFT), the Vienna ab initio Simulation Package (VASP) was performed to evaluate Gibbs free energy and the density of states (DOS). [1] Meanwhile, the exchange-correlation energy was investigated using the generalized gradient approximation (GGA) with the Perdew-Burke-Ernzerhof (PBE) function. [2] The plane-wave cutoff energy was set at 400 eV. An atomic force convergence criterion of 0.001

eV $Å^{-1}$ was used to identify the optimized geometry. Furthermore, models of the surface plates were constructed with an ample vacuum space of 15 Å to avoid the interaction of the different plates. The Brillouin zone was sampled using a single gamma grid for geometry optimization. The DFT-D3 dispersion correction method was used to illustrate the weak interaction between the slab and the active species. [3]

4. Theoretical models:

The OER cycle proposed by precious work. [4-8] In detail, For OER in alkaline electrolyte (pH=14), since OH^- may act as an electron donor, the overall reaction scheme of OER can be expressed as:

$$OH^- + * \rightarrow OH^* + e^- \quad (1)$$

$$OH^* + OH^- \rightarrow O^* + H_2O\ (l) + e^- \quad (2)$$

$$O^* + OH^- \rightarrow OOH^* + e^- \quad (3)$$

$$OOH^* + OH^- \rightarrow O_2(g) + H_2O(l) + e^- + * \quad (4)$$

For each elementary step associated with OER, the Gibbs reaction free energy ΔG is defined as the difference between free energies of the initial and final states, given by the following expression:

$$\Delta G = \Delta E + \Delta ZPE - T\Delta S \quad (5)$$

where ΔE is the reaction energy of reactant and product molecules adsorbed on catalyst surface, and ΔZPE and ΔS are the change in zero-point energies and entropy in the reaction.

The reaction free energy of (1)-(4) for the OER can be determined from the following equations:

$$OH^- + * \rightarrow OH^* + e^-$$

$\Delta G_1 = G_{OH*} + G_{e-} - G_{OH-} - G_*$

$= G_{OH*} + G_{e-} - (G_{H2O}(l) + G_{e-} - 1/2G_{H2}(g)) - G_*$

$= G_{OH*} + 1/2G_{H2}(g) - G_{H2O}(l) - G_*$

$= \Delta G_{OH*}$ (6)

$OH^* + OH^- \rightarrow O^* + H_2O + e^-$

$\Delta G_2 = G_{O*} + G_{H2O} + G_{e-} - G_{OH-} - G_{OH*}$

$= G_{O*} + G_{H2O} + G_{e-} - [G_{H2O}(l) + G_{e-} - 1/2G_{H2}(g)] - G_{OH*}$

$= (G_{O*} + G_{H2} - G_{H2O}(l) - G_*) - (G_{OH*} + 1/2G_{H2}(g) - G_{H2O}(l) - G_*)$

$= \Delta G_{O*} - \Delta G_{OH*}$ (7)

$O^* + OH^- \rightarrow OOH^* + e^-$

$\Delta G_3 = G_{OOH*} + G_{e-} - G_{O*} - G_{OH-}$

$= G_{OOH*} + G_{e-} - G_{O*} - (G_{H2O}(l) + G_{e-}1/2G_{H2}(g))$

$= (G_{OOH*} + 3/2G_{H2}(g) - 2G_{H2O}(l) - G_*) - (G_{O*} + G_{H2}(g) - G_{H2O}(l) - G_*)$

$= \Delta G_{OOH*} - \Delta G_{O*}$ (8)

$OOH^* + OH^- \rightarrow O_2(g) + H_2O(l) + e^- + *$

$\Delta G_4 = G_{O2}(g) + G_{H2O}(l) + G_{e-} + * - G_{OOH*} - G_{OH-}$

$= (2G_{H2O}(l) - 2G_{H2}(g) + 4 \times 1.23) + G_{H2O}(l) + G_{e-}$

$+ * - G_{OOH*} - (G_{H2O}(l) + G_{e-} - 1/2G_{H2}(g))$

$= 2G_{H2O}(l) - 1/2G_{H2}(g) + * - G_{OOH*}$

$= 4.92 - \Delta G_{OOH*}$ (9)

With this method, the theoretical overpotential (U^{OER}) at standard condition is defined as:

$$U^{OER} = (G^{OER} / e) - 1.23 \quad (10)$$

where G^{OER} is the potential determining step defined as the highest free-energy step in the OER, and e is unit charge.

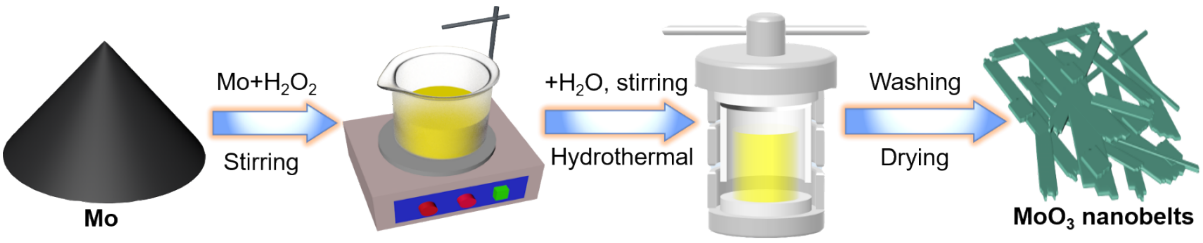

Figure S1. Schematic illustration of the formation for MoO_3 nanobelts.

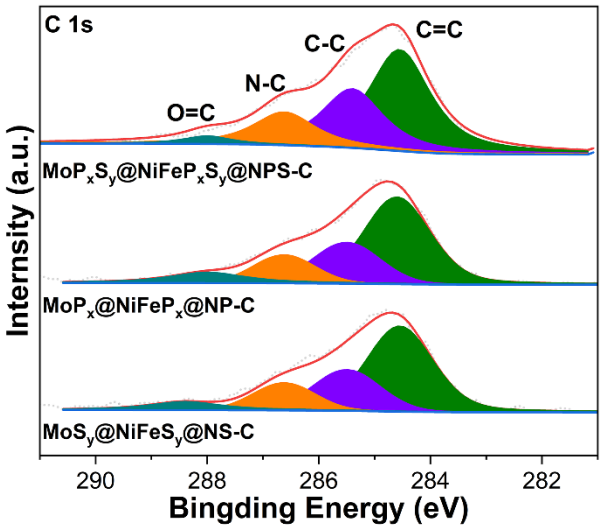

Figure S2. XPS spectra of C 1s for MoS_y@$NiFeS_y$@NS-C, MoP_x@$NiFeP_x$@NP-C, and MoP_xS_y@$NiFeP_xS_y$@NPS-C catalysts.

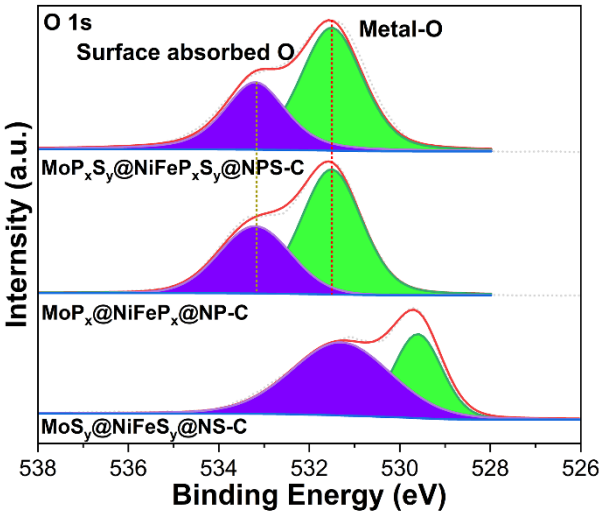

Figure S3. XPS spectra of O 1s for MoS_y@$NiFeS_y$@NS-C, MoP_x@$NiFeP_x$@NP-C, and MoP_xS_y@$NiFeP_xS_y$@NPS-C catalysts.

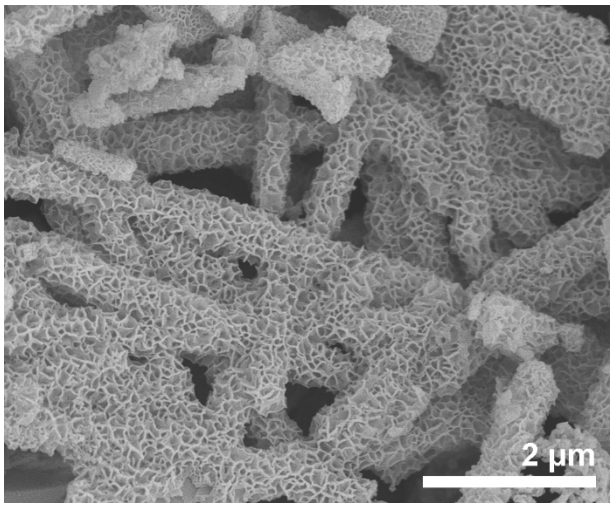

Figure S4. SEM images of MoO_3@$Ni(OH)_2$.

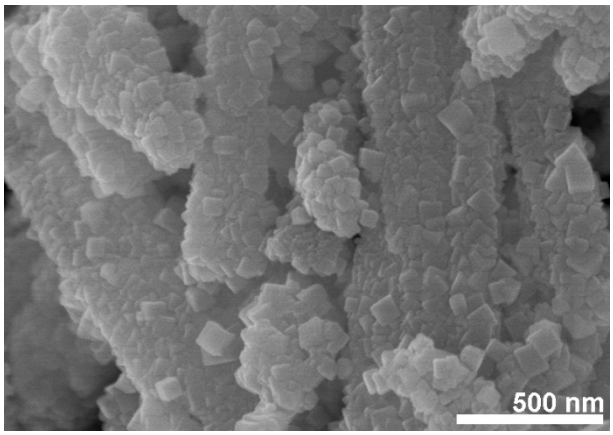

Figure S5. SEM images of MoO_3@$Ni(OH)_2$@NiFe-PB.

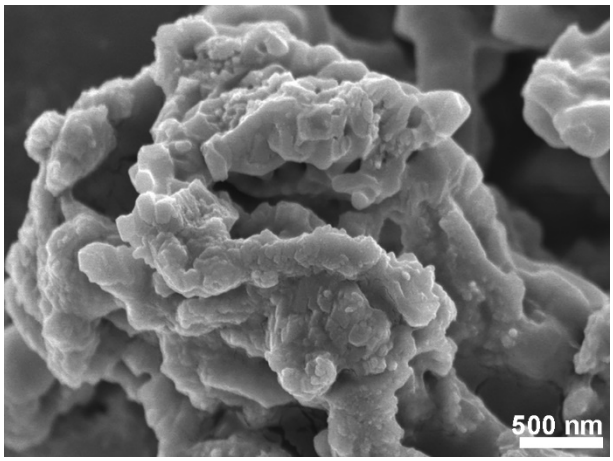

Figure S6. SEM images of MoP_xS_y@$NiFeP_xS_y$@NPS-C.

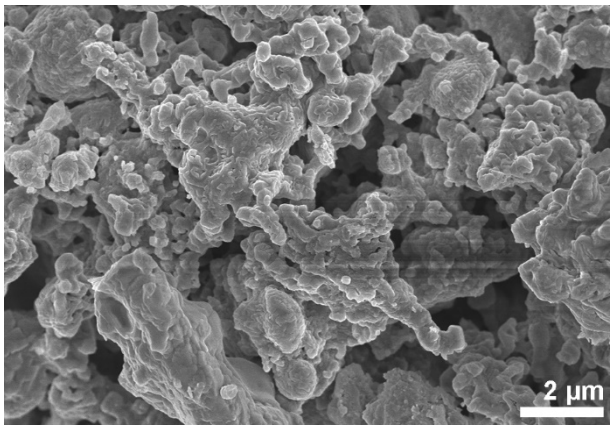

Figure S7. SEM images of MoP_x@$NiFeP_x$@NP-C.

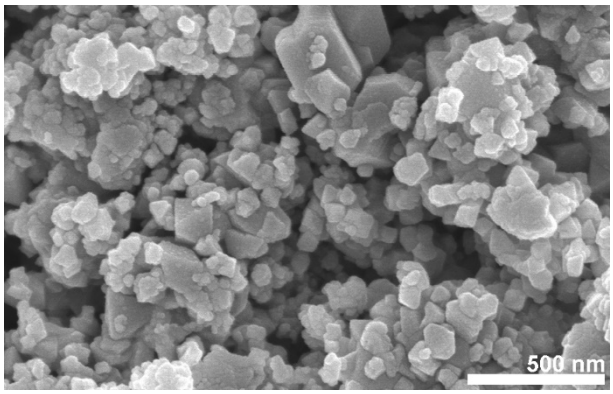

Figure S8. SEM images of MoS_y@$NiFeS_y$@NS-C.

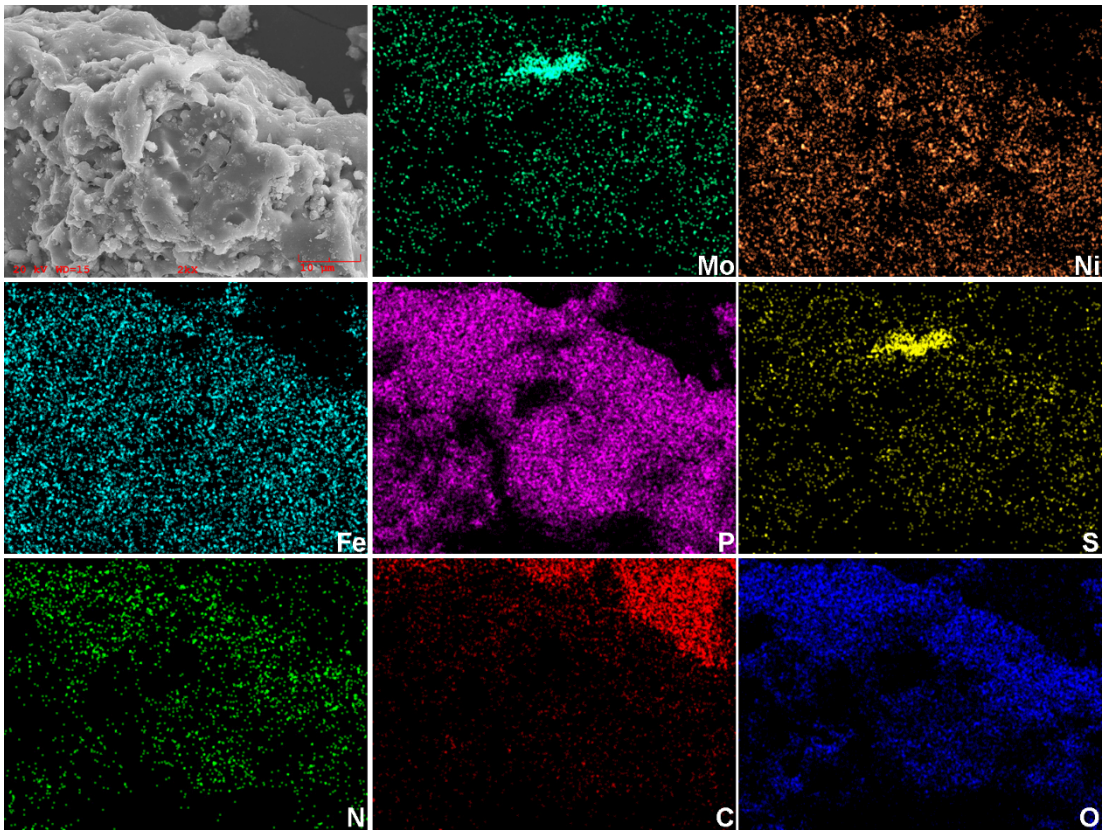

Figure S9. Elemental mapping of MoP_xS_y@$NiFeP_xS_y$@NPS-C.

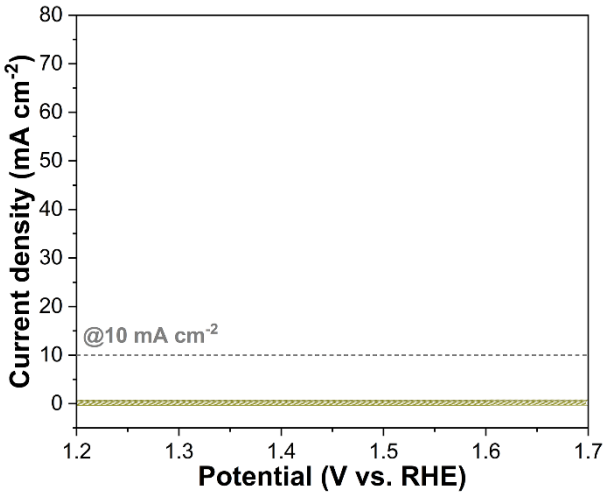

Figure S10. LSV curves MoO_3 nanobelts after phosphorization and sulfurization.

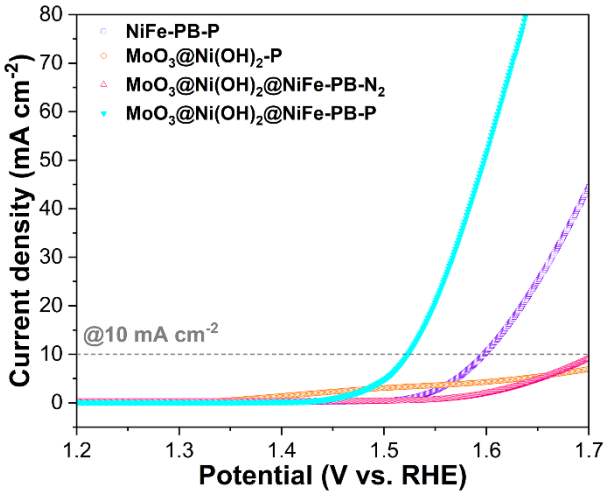

Figure S11. LSV curves of MoO_3@$Ni(OH)_2$@NiFe-PB after direct heat treatment, NiFe-PB, MoO_3@$Ni(OH)_2$, and MoO_3@$Ni(OH)_2$@NiFe-PB after phosphorization.

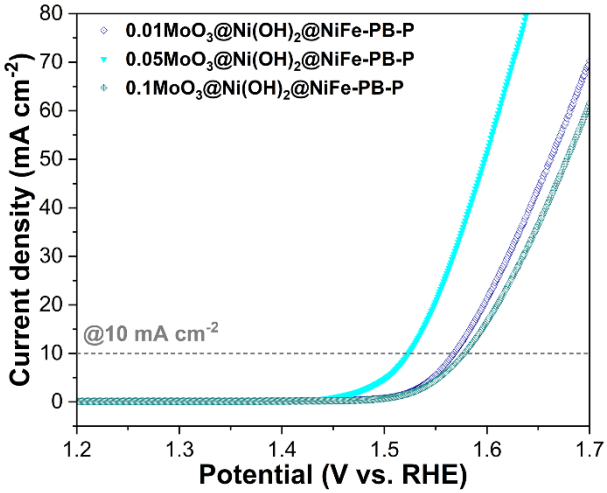

Figure S12. LSV curves of MoO_3@$Ni(OH)_2$@NiFe-PB with different MoO_3 contents after phosphorization.

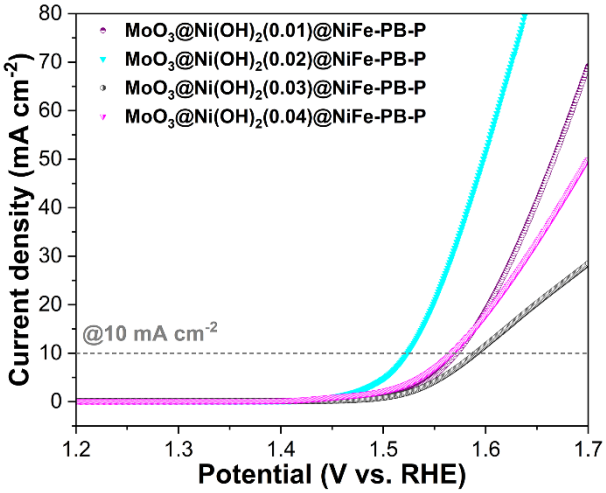

Figure S13. LSV curves of MoO_3@$Ni(OH)_2$@NiFe-PB with different MoO_3@$Ni(OH)_2$ contents after phosphorization.

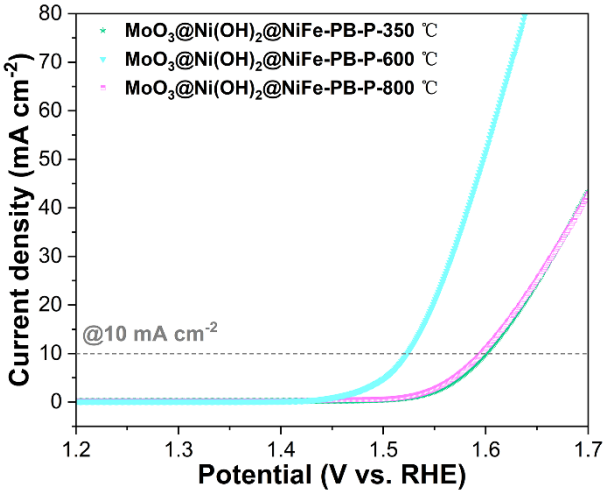

Figure S14. LSV curves of MoO_3@$Ni(OH)_2$@NiFe-PB at different phosphating temperatures.

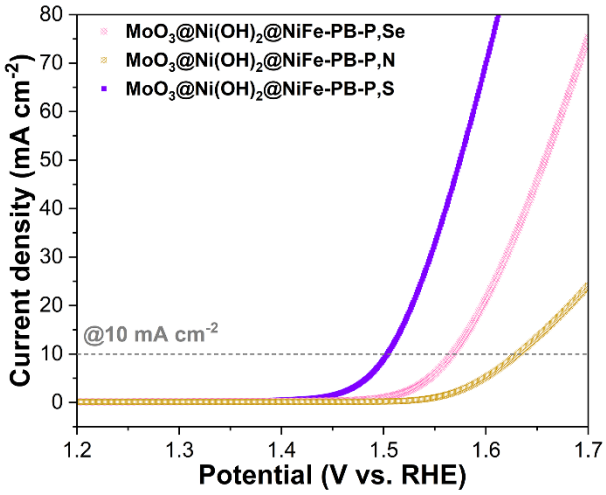

Figure S15. LSV curves of MoO_3@$Ni(OH)_2$@NiFe-PB doped with different elements (N, P, Se).

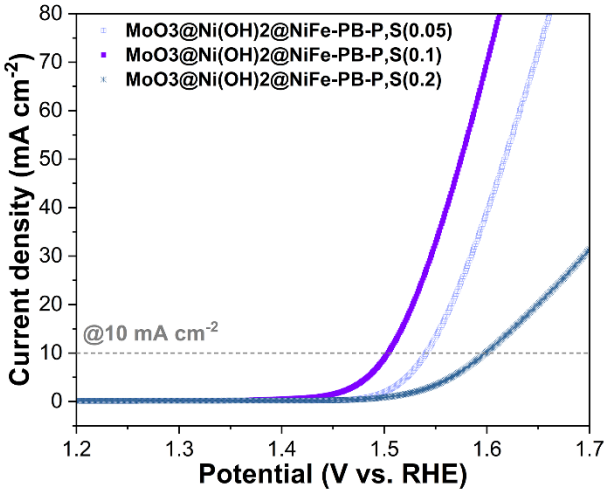

Figure S16. LSV curves of MoO_3@$Ni(OH)_2$@NiFe-PB with different thiourea contents after phosphorization and sulfurization.

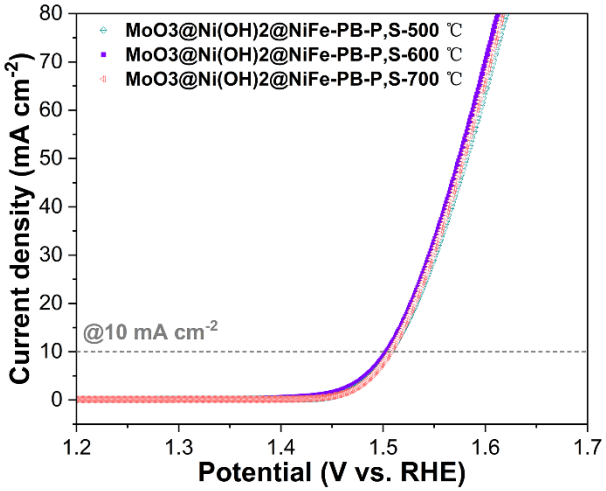

Figure S17. LSV curves of MoO_3@$Ni(OH)_2$@NiFe-PB heat-treated at different temperatures during phosphorization and sulfurization.

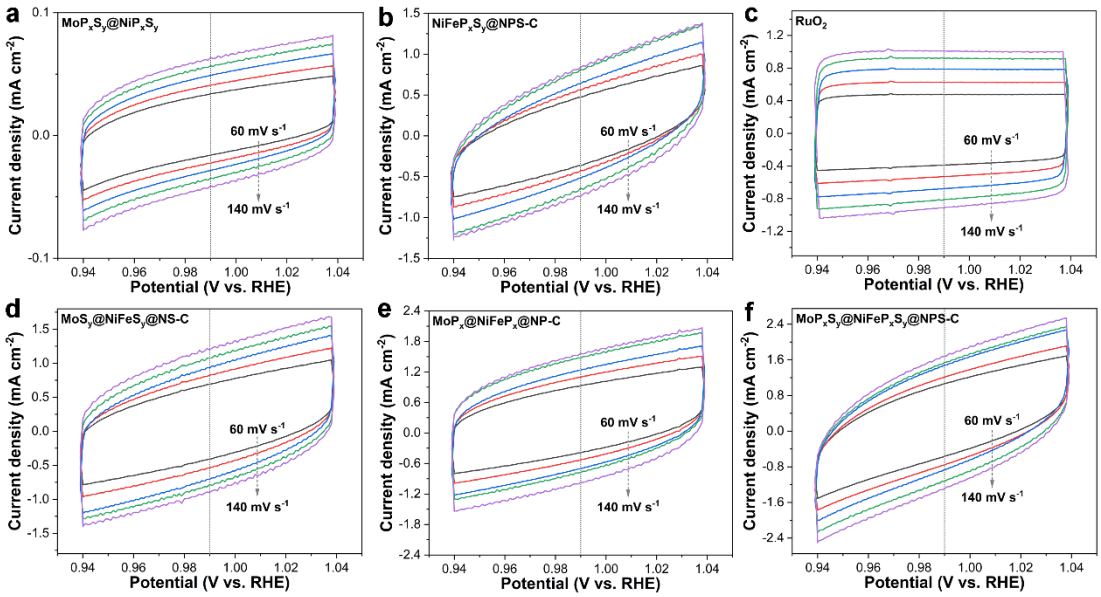

Figure S18. CV curves at different scan rates (60-140 mV s^{-1} with the interval of 20 mV s^{-1}) of (a) MoP_xS_y@NiP_xS_y, (b) $NiFeP_xS_y$@NPS-C, (c) commercial RuO_2, (d) MoS_y@$NiFeS_y$@NS-C, (e) MoP_x@$NiFeP_x$@NP-C, (f) MoP_xS_y@$NiFeP_xS_y$@NPS-C catalysts during OER process under 1 M KOH solution.

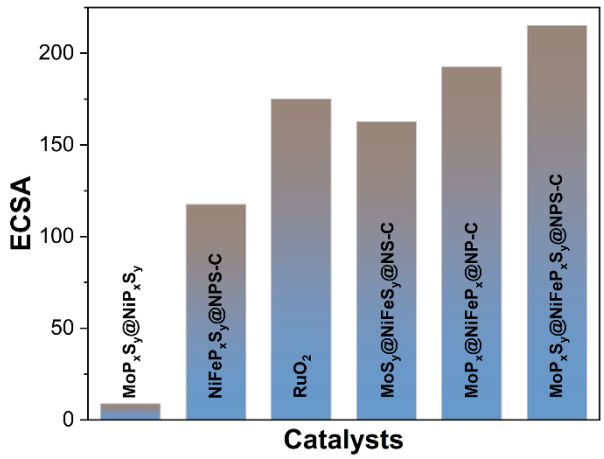

Figure S19. ECSA values of MoP_xS_y@NiP_xS_y, $NiFeP_xS_y$@NPS-C, commercial RuO_2, MoS_y@$NiFeS_y$@NS-C, MoP_x@$NiFeP_x$@NP-C, MoP_xS_y@$NiFeP_xS_y$@NPS-C catalysts.

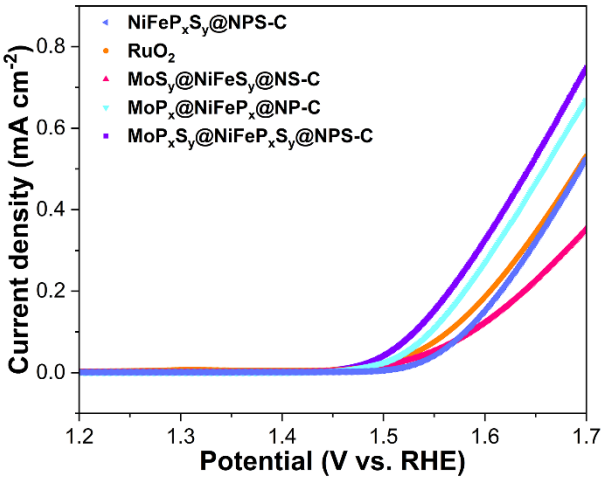

Figure S20. ECSA-normalized LSV curves of $NiFeP_xS_y$@NPS-C, commercial RuO_2, MoS_y@$NiFeS_y$@NS-C, MoP_x@$NiFeP_x$@NP-C, MoP_xS_y@$NiFeP_xS_y$@NPS-C catalysts.

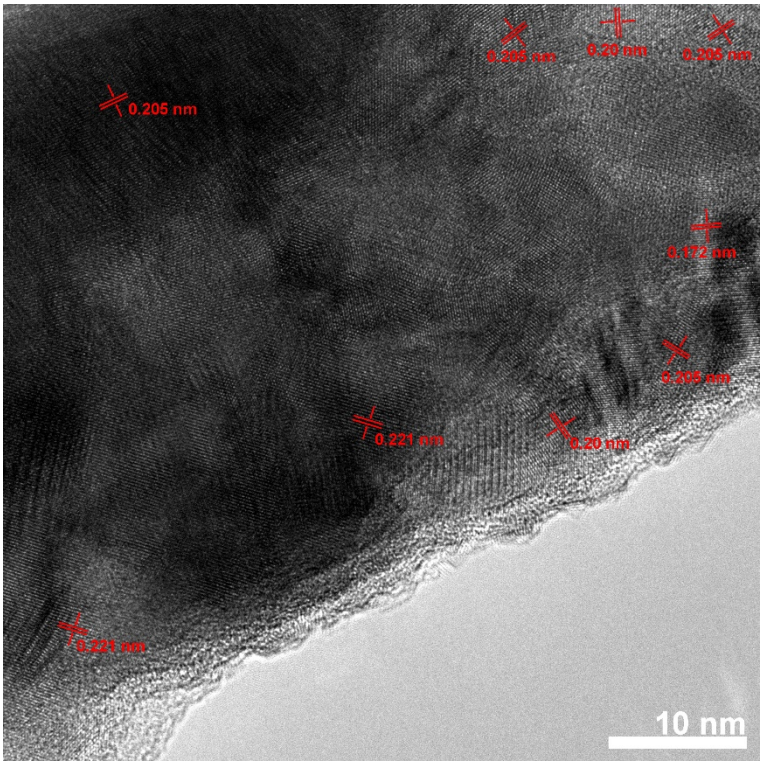

Figure S21. HRTEM image of MoP_xS_y@$NiFeP_xS_y$@NPS-C catalyst after long-term stability test.

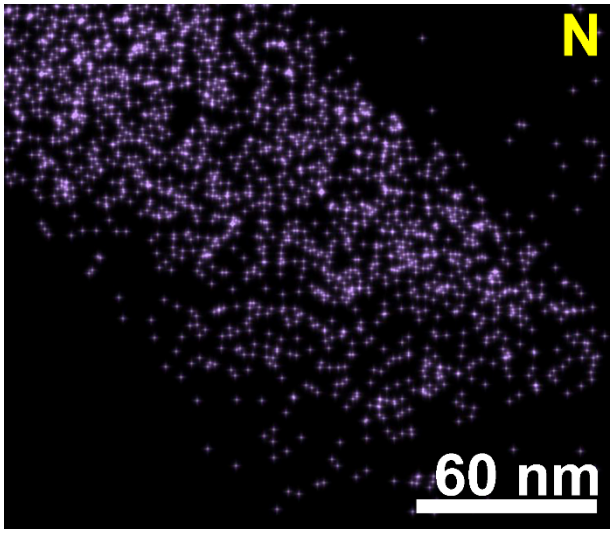

Figure S22. Elemental mapping of N for MoP_xS_y@$NiFeP_xS_y$@NPS-C catalyst.

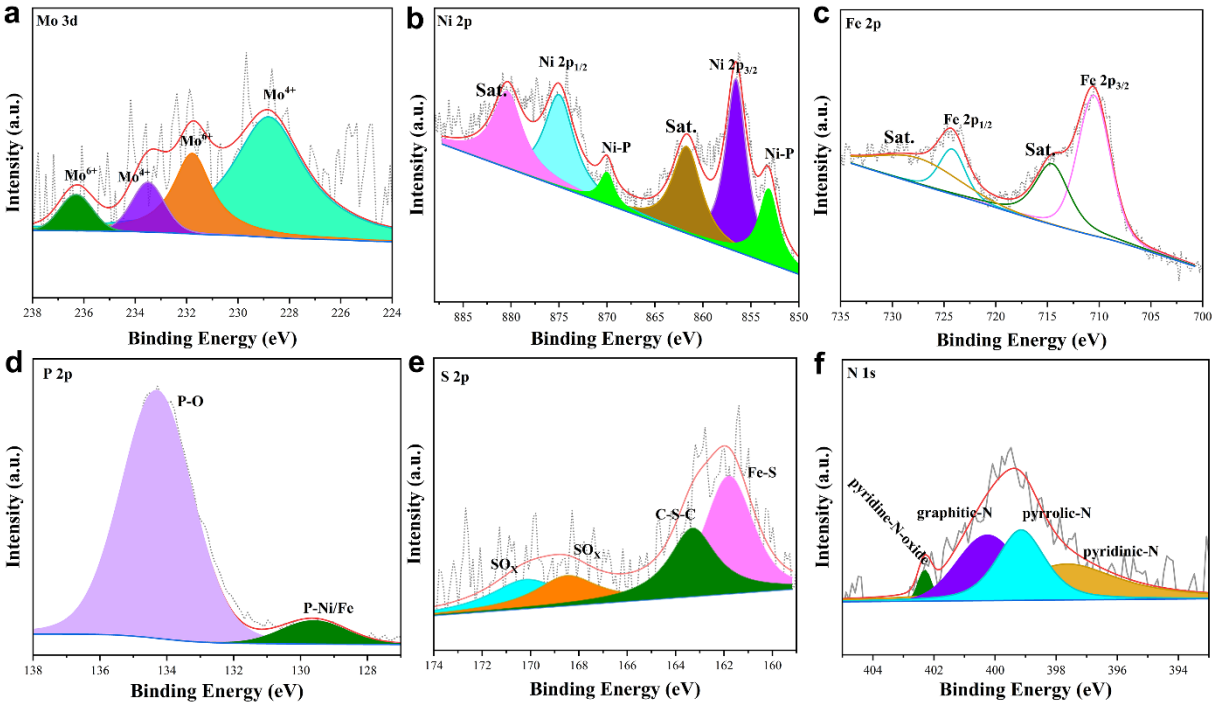

Figure S23. XPS spectra of (a) Mo 3d, (b) Ni 2p, (c) Fe 2p, (d) P 2p, (e) S 2p, and (f) N 1s for MoP_xS_y@$NiFeP_xS_y$@NPS-C catalyst after long-term stability test.

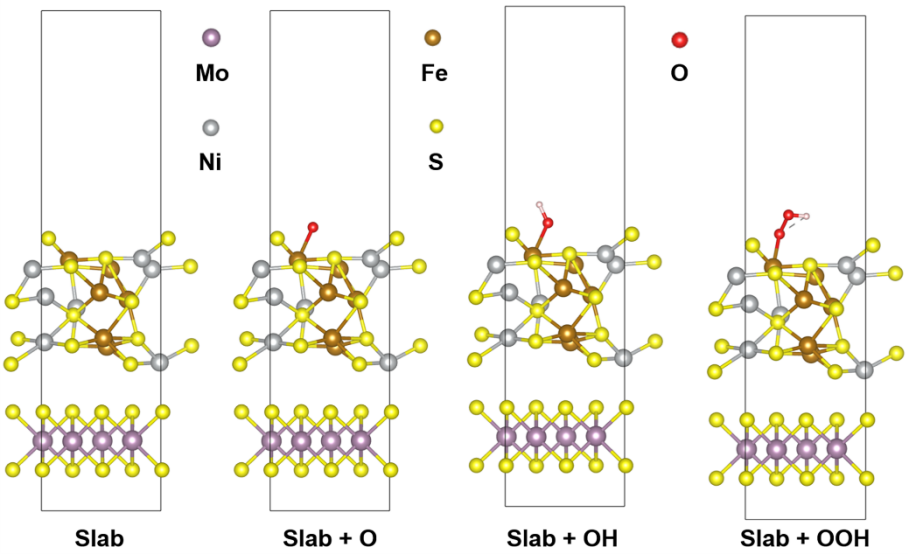

Figure S24. Optimized structures models of MoS_y@$NiFeS_y$@NS-C for adsorption of intermediates (*O, *OH, and *OOH) under OER in an alkaline media.

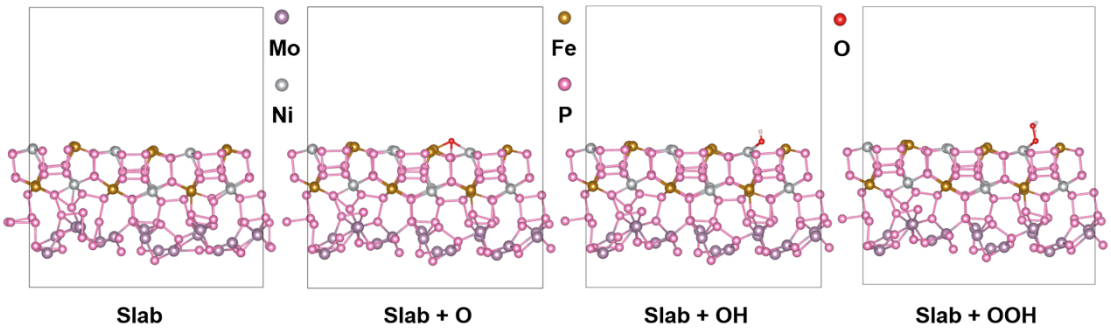

Figure S25. Optimized structures models of MoP_x@$NiFeP_x$@NP-C for adsorption of intermediates (*O, *OH, and *OOH) under OER in an alkaline media.

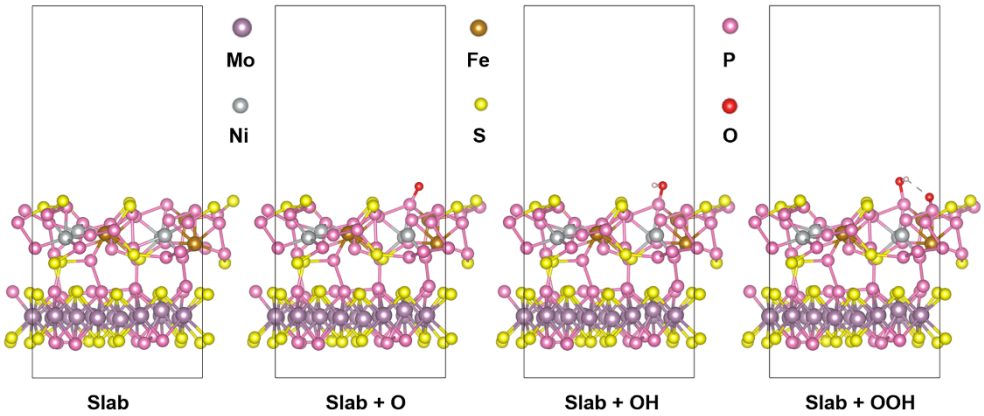

Figure S26. Optimized structures models of MoP_xS_y@$NiFeP_xS_y$@NPS-C for adsorption of intermediates (*O, *OH, and *OOH) under OER in an alkaline media.

Table S1. Element contents in the MoP_xS_y@$NiFeP_xS_y$@NPS-C heterostructures detected by XPS technique.

Elements	Atomic %
C	15.09
S	0.28
P	18.68
O	56.77
N	2.4
Mo	0.09
Ni	2.87
Fe	3.82

Table S2. Element contents in the MoP_xS_y@$NiFeP_xS_y$@NPS-C heterostructures detected by ICP-OES technique.

Elements	mass %
P	24.4
S	0.4
Mo	0.4
Ni	18.54
Fe	12.36

Table S3. Electrocatalytic performances toward OER of MoP_xS_y@$NiFeP_xS_y$@NPS-C heterostructure and recently advanced noble metal-free catalysts.

Electrocatalysts	Loading (mg cm^{-2})	OER η (mV) @10 mA cm^{-2}	Electrolyte	Ref.
$MnS_{0.1}O_{1.9}/MnCo_2S_4$	0.26	414	1 M KOH	[9]
$CeO_2/Co(OH)_2$	-	410	1 M KOH	[10]
ACTP5@Co,N-800	0.30	374	0.1 M KOH	[11]
Co/CeO_2	0.11	365	1 M KOH	[12]
Co_2P	0.17	364	1 M KOH	[13]
CoV_2O_6	0.23	360	1 M KOH	[14]
BP-CN-c	0.50	350	1 M KOH	[15]
MnSAC	0.10	350	0.1 M KOH	[16]
$Ni_{1.4}Co_{1.6}O_4$	2.00	350	1 M KOH	[17]
$NiCo_2O_4$	-	350	1 M KOH	[18]
DE-TDAP	-	346	0.1 M KOH	[19]
$NiCo_2S_4$	1.00	338	0.1 M KOH	[20]

Co-Ni (Trace)/NCNTs	0.56	337	0.1 M KOH	[21]
Ni/$FeSe_2$		330	1 M KOH	[22]
$Ni_3V_2O_8$	0.19	328	1 M KOH	[23]
$Sr_2Fe_{1.5}Mo_{0.5}O_{6-\delta}$	0.23	322	1 M KOH	[24]
Ni-Co_3O_4	-	321	1 M KOH	[25]
GNiPy350N	-	320	1 M KOH	[26]
MOF-D $CoSe_2$	0.25	320	1 M KOH	[27]
3D porous MOFs	0.50	320	1 M KOH	[28]
Co-N/S/rGO	2.00	320	1 M KOH	[29]
$Co_{0.9}1Fe_{0.09}O$-N	0.71	319	1 M KOH	[30]
CoMo-MI-600	-	316	1 M KOH	[31]
CoFe PBA@CoP/NF	-	312	1 M KOH	[32]
Ni-N-CNT@Co_3O_4	-	310	1 M KOH	[33]
Fe-Co-CN/rGO-700	0.25	308	1 M KOH	[34]
Mo_2C/Co@NC	1.00	308	1 M KOH	[35]
CoSA/N,S-HCS	1.50	306	1 M KOH	[36]
Ni/polyTACoPc	-	304	1 M KOH	[37]
$Ni_{0.3}Co_{0.7}$-9AC-AD/NF	-	300	1 M KOH	[38]
Ni_xS_y@MnO_xH_y	-	299	1 M KOH	[39]
Ni-Fe-S/3NCQDs	1.19	295	0.1 M KOH	[40]
LC-CoOOH NAs/CFC	-	294	1 M KOH	[41]
g-C_3N_4/$NiCo_2O_4$	0.20	294	1 M KOH	[42]
Vo-$MnCo_2O_4$	0.40	290	1 M KOH	[43]
P-Co_3O_4	0.30	290	1 M KOH	[44]
$Se_{1.0}$-Co_3S_4-$V_{S/Se}$-V_{Co}	-	289.5	0.1 M KOH	[45]
FeNi-Mo_2C/C	0.07	288	1 M KOH	[46]
CoFe-P/NF	-	287	1 M KOH	[47]
NiFeP/MXene	0.25	286	1 M KOH	[48]
Ni/Ni_2P@N-CNF	0.25	285	1 M KOH	[49]
MoP_xS_y@$NiFeP_xS_y$@NPS	0.20	274	1 M KOH	This work
$NiCo_{2-x}Fe_xO_4$	0.50	274	1 M KOH	[50]

Fe-Co-O/Co@NC-	-	257	1 M KOH	[51]
Co-C@NiFe LDH	0.82	249	1 M KOH	[52]

References

[1] G. Kresse, J. Hafner, Ab initio molecular dynamics for liquid metals, *Phy. Rev. B* 1993, **47**, 558.

[2] X. J. Zeng, J. L. Shui, X. F. Liu, Q. T. Liu, Y. C. Li, J. X. Shang, L. R. Zheng, R. H. Yu, Single-atom to single-atom grafting of Pt_1 onto Fe-N_4 center: Pt_1@Fe-N-C multifunctional electrocatalyst with significantly enhanced properties, *Adv. Energy Mater.* 2018, **8**, 1701345.

[3] G. Kresse, J. Furthmüller, Efficient iterative schemes for ab initio total-energy calculations using a plane-wave basis set, *Phy. Rev. B* 1996, **54**, 11169.

[4] J. Rossmeisl, Z.-W. Qu, H. Zhu, G.-J. Kroes, J. K. Nørskov, Electrolysis of Water on Oxide Surfaces, *J. Electroanal. Chem.* 2007, **607**, 83–89.

[5] J. Rossmeisl, A. Logadottir, J. K. Nørskov, Electrolysis of Water on (Oxidized) Metal Surfaces, *Chem. Phys.* 2005, **319**, 178–184.

[6] I. C. Man, H.-Y. Su, F. Calle-Vallejo, H. A. Hansen, J. I. Martínez, N. G. Inoglu, J. Kitchin, T. F. Jaramillo, J. K. Nørskov, J. Rossmeisl, Universality in Oxygen Evolution Electrocatalysis on Oxide Surfaces, *ChemCatChem* 2011, **3**, 1159–1165.

[7] Larsson E. An X-ray investigation of Ni-P system and crystal structures of NiP and NiP_2, Arkiv for Kemi 1965, **23**, 335.

[8] P. Wang, X. Zhang, J. Zhang, S. Wan, S. Guo, G. Lu, J. Yao, X. Huang, Precise tuning in platinum-nickel/nickel sulfide interface nanowires for synergistic hydrogen evolution catalysis, *Nat. Commun.* 2017, **8**, 14580.

[9] K. Wang, Z. Wang, Y. G. Liu, J. P. Liu, Z. M. Cui, X. F. Zhang, F. Ciucci, Z. H. Tang, Tailoring the interfacial active center of $MnS_xO_{2-x}/MnCo_2S_4$ heterostructure to boost the performance for oxygen evolution reaction and Zn-Air batteries in neutral electrolyte, *Chem. Eng. J.* 2022, **427**, 131966.

[10] M. C. Sung, G. H. Lee, D. W. Kim, $CeO_2/Co(OH)_2$ hybrid electrocatalysts for efficient hydrogen and oxygen evolution reaction, *J. Alloy. Compd.* 2019, **800**, 450–455.

[11] J. T. Zhang, T. Zhang, J. Ma, Z. Wang, J. H. Liu, X. Z. Gong, ORR and OER of Co-N codoped carbon-based electrocatalysts enhanced by boundary layer oxygen molecules transfer, *Carbon* 2021, **172**, 556–568.

[12] M. Akbayrak, A. M. Önal, Metal oxides supported cobalt nanoparticles: Active electrocatalysts for oxygen evolution reaction, *Electrochim. Acta* 2021, **393**, 139053.

[13] B. T. Jebaslinhepzybai, T. Partheeban, D. S. Gavali, R. Thapa, M. Sasidharan, One-pot solvothermal synthesis of Co_2P nanoparticles: An efficient HER and OER electrocatalysts, *Int. J. Hydrog. Energy* 2021, **46**, 21924–21938.

[14] A. Mondal, S. Ganguli, H. R. Inta, V. Mahalingam, Influence of Vanadate Structure on Electrochemical Surface Reconstruction and OER Performance of CoV_2O_6 and $Co_3V_2O_8$, *ACS Appl. Energy Mater.* 2021, **4**, 5381–5387.

[15] X. Wang, R. K. M. Raghupathy, C. J. Querebillo, Z. Q. Liao, D. Q. Li, K. Lin, M. Hantusch, Z. Sofer, B. H. Li, E. Zschech, I. M. Weidinger, T. D. Kühne, H. Mirhosseini, M. H. Yu, X. L. Feng, Interfacial Covalent Bonds Regulated Electron-Deficient 2D Black Phosphorus for Electrocatalytic Oxygen Reactions, *Adv. Mater.* 2021, **33**, 2008752.

[16] H. S. Shang, W. M. Sun, R. Sui, J. J. Pei, L. R. Zheng, J. C. Dong, Z. L. Jiang, D. N. Zhou, Z. B. Zhuang, W. X. Chen, J. T. Zhang, D. S. Wang, Y. D. Li, Engineering Isolated Mn-N_2C_2 Atomic Interface Sites for Efficient Bifunctional Oxygen Reduction and Evolution Reaction, *Nano Lett.* 2020, **20**, 5443c5450.

[17] C. Broicher, M. Klingenhof, M. Frisch, S. Dresp, N. M. Kubo, J. Artz, J. Radnik, S. Palkovits, A. K. Beine, P. Strasser, R. Palkovits, Particle size-controlled synthesis of high-performance MnCo-based materials for alkaline OER at fluctuating potentials, *Catal. Sci. Technol.* 2021, **11**, 7278–7286.

[18] C. Broicher, F. Zeng, J. Artz, H. Hartmann, A. Besmehn, S. Palkovits, R. Palkovits, Facile synthesis of mesoporous nickel cobalt oxide for OER-insight into intrinsic electrocatalytic activity, *ChemCatChem* 2019, **11**, 412–416.

[19] A. Bahadur, W. Hussain, S. Iqbal, F. Ullah, M. Shoaib, G. C. Liu, K. J. Feng, A morphology controlled surface sulfurized $CoMn_2O_4$ microspike electrocatalyst for water splitting with excellent OER rate for binder-free electrocatalytic oxygen evolution, *J. Mater. Chem. A* 2021, **9**, 12255–12264.

[20] S. Sarawutanukul, C. Tomon, S. Duangdangchote, N. Phattharasupakun, M. Sawangphruk, S. Duangdangchote, Rechargeable photoactive Zn-air batteries using $NiCo_2S_4$ as an efficient bifunctional photocatalyst towards OER/ORR at the cathode, *Batteries & Supercaps* 2020, **3**, 541–547.

[21] Y. D. Shi, J. N. Cai, X. F. Zhang, Z. S. Li, S. Lin, Promotional effects of trace Ni on its dual-functional electrocatalysis of Co/N-doped carbon nanotube catalysts for ORR and OER, *Int. J. Hydrog. Energy* 2022, **47**, 7761–7769.

[22] R. Gao, H. Zhang, D. Yan, Iron diselenide nanoplatelets: Stable and efficient water-electrolysis catalysts, *Nano Energy* 2017, **31**, 90–95.

[23] R. Biswas, A. Kundu, M. Saha, V. Kaur, B. Banerjee, R. S. Dhayal, R. A. Patil, Y. R. Ma, T. Sen, K. K. Haldar, Rational design of marigold-shaped composite $Ni_3V_2O_8$ flowers: a promising catalyst for the oxygen evolution reaction, *New J. Chem.* 2020, **44**, 12256–12265.

[24] B. B. He, K. Tan, Y. S. Gong, R. Wang, H. W. Wang, L. Zhao, Coupling amorphous cobalt hydroxide nanoflakes on $Sr_2Fe_{1.5}Mo_{0.5}O_{5+\delta}$ perovskite nanofibers to induce bifunctionality for water splitting, *Nanoscale* 2020, **12**, 9048–9057.

[25] H. Du, W. H. Pu, C. Z. Yang, Morphology control of Co_3O_4 with nickel incorporation for highly efficient oxygen evolution reaction, *Appl. Surf. Sci.* 2021, **541**, 148221.

[26] Souza, A. S.; Bezerra, L. S.; Cardoso, E. S. F.; Fortunato, G. V.; Maia, G. Nickel pyrophosphate combined with graphene nanoribbon used as efficient catalyst for OER, *J. Mater. Chem. A* 2021, **9**, 11255–11267.

[27] N. Sahu, J. K. Das, J. N. Behera, Metal-organic framework (MOF) derived flower-shaped $CoSe_2$ nanoplates as a superior bifunctional electrocatalyst for both oxygen and hydrogen evolution reactions, *Sustain. Energy Fuels* 2021, **5**, 4992–5000.

[28] Q. Qiu, T. Wang, L. H. Jing, K. Huang, D. B. Qin, Tetra-carboxylic acid based metal-organic framework as a high-performance bifunctional electrocatalyst for HER and OER, *Int. J. Hydrog. Energy* 2020, **45**, 11077–11088.

[29] L. Gu, X. L. Sun, J. Zhao, B. Q. Gong, Z. L. Bao, H. L. Jia, M. Y. Guan, S. S. Ma, A highly efficient bifunctional electrocatalyst (ORR/OER) derived from GO functionalized with carbonyl, hydroxyl and epoxy groups for rechargeable zinc-air batteries, *New J. Chem.* 2021, **45**, 6535–6542.

[30] Q. G. Du, P. P. Su, Z. Z. Cao, J. Yang, C. A. H. Price, J. Liu, Construction of N and Fe co-doped CoO/Co_xN interface for excellent OER performance, *Sustain. Mater. Techno.* 2021, **29**, e00293.

[31] Y. Y. Guo, Q. Huang, J. Y. Ding, L. Zhong, T. T. Li, J. Q. Pan, Y. Hu, J. J. Qian, S. M. Huang, CoMo carbide/nitride from bimetallic MOF precursors for enhanced OER performance, *Int. J. Hydrog. Energy* 2021, **46**, 22268–22276.

[32] L. Quan, S. H. Li, Z. P. Zhao, J. Q. Liu, Y. Ran, J. Y. Cui, W. Lin, X. L. Yu, L. Wang, Y. H. Zhang, J. H. Ye, Hierarchically Assembling CoFe Prussian Blue Analogue Nanocubes on CoP Nanosheets as Highly Efficient Electrocatalysts for Overall Water Splitting, *Small Methods* 2021, **5**, 2100125.

[33] J. Wu, Y. Liu, D. Geng, H. Liu, X. Meng, Cobalt oxide nanosheets anchored onto nitrogen-doped carbon nanotubes as dual purpose electrodes for lithium-ion batteries and oxygen evolution reaction, *Int. J. Energy. Res.* 2018, **42**, 853–862.

[34] W. H. Fang, J. Wang, Y. Hu, X. Q. Cui, R. F. Zhu, Y. H. Zhang, C. C. Yue, J. Q. Dang, W. Cui, H. Zhao, Z. X. Li, Metal-Organic Framework Derived Fe-Co-CN/Reduced Graphene Oxide for Efficient HER and OER, *Electrochim. Acta* 2021, **365**, 137384.

[35] T. T. Gu, R. J. Sa, L. J. Zhang, D. S. Li, R. H. Wang, Engineering interfacial coupling between Mo_2C nanosheets and Co@NC polyhedron for boosting electrocatalytic water splitting and zinc-air batteries, *Appl. Catal. B* 2021, **296**, 120360.

[36] Z. Y. Zhang, X. X. Zhao, S. B. Xi, L. L. Zhang, Z. X. Chen, Z. P. Zeng, M. Huang, H. B. Yang, B. Liu, S. J. Pennycook, P. Chen, Atomically Dispersed Cobalt Trifunctional Electrocatalysts with Tailored Coordination Environment for Flexible Rechargeable Zn-Air Battery and Self-Driven Water Splitting, *Adv. Energy Mater.* 2020, **10**, 2002896.

[37] S. Aralekallu, V. A. Sajjan, M. Palanna, K. Prabhu C P, M. Hojamberdiev, L. K. Sannegowda, Ni foam-supported azo linkage cobalt phthalocyanine as an efficient electrocatalyst for oxygen evolution reaction, *J. Power Sources* 2020, **449**, 227516.

[38] W. Ye, Y. S. Yang, X. Y. Fang, M. Arif, X. B. Chen, D. P. Yan, 2D cocrystallized metal-organic nanosheet array as an efficient and stable bifunctional electrocatalyst for overall water splitting, *ACS Sustainable Chem. Eng.* 2019, **7**, 18085–18092.

[39] P. Wang, Y. Z. Luo, G. X. Zhang, Z. S. Chen, H. Ranganathan, S. H. Sun, Z. C. Shi, Interface Engineering of Ni_xS_y@MnO_xH_y Nanorods to Efficiently Enhance Overall-Water-Splitting Activity and Stability, *Nano-Micro Lett.* 2022, **14**, 120.

[40] R. Y. Wang, J. Liu, J. H. Xie, Z. Cai, Y. Yu, Z. X. Zhang, X. Meng, C. Wang, X. Q. Xu, J. L. Zou, Hollow nanocage with skeleton Ni-Fe sulfides modified by N-doped carbon quantum dots for enhancing mass transfer for oxygen electrocatalysis in zinc-air battery, *Appl. Catal. B* 2023, **324**, 122230.

[41] S. H. Ye, J. P. Wang, J. Hu, Z. D. Chen, L. R. Zheng, Y. H. Fu, Y. Q. Lei, X. Z. Ren, C. X. He, Q. L. Zhang, J. H. Liu, Electrochemical Construction of Low-Crystalline CoOOH Nanosheets with Short-Range Ordered Grains to Improve Oxygen Evolution Activity, *ACS Catal.* 2021, **11**, 6104–6112.

[42] X. J. Zeng, Q. Q. Zhang, Z.-Y. Shen, H. Q. Zhang, T. Wang, Z. Y. Liu, Doping and vacancy engineering in sandwich-like g-C_3N_4/$NiCo_2O_4$ heterostructure for robust oxygen evolution, *ChemNanoMat*, 2022, **8**, e202200191.

[43] K. Zeng, W. Li, Y. Zhou, Z. H. Sun, C. Y. Lu, J. Yan, J. H. Choi, R. Z. Yang, Multilayer Hollow $MnCo_2O_4$ Microsphere with Oxygen Vacancies as Efficient Electrocatalyst for Oxygen Evolution Reaction, *Chem. Eng. J.* 2021, **421,** 127831.

[44] Y. Lu, C. J. Li, Y. Zhang, X. Cao, G. Xie, M. L. Wang, D. D. Peng, K. Huang, B. W. Zhang, T. Wang, J. S. Wu, Y. Z. Huang, Engineering of cation and anion vacancies in Co_3O_4 thin nanosheets by laser irradiation for more advancement of oxygen evolution reaction, *Nano Energy* **2021**, *83*, 105800.

[45] X. Y. Gu, S. S. Li, W.Q. Shao, X. Q. Mu, Y. X. Yang, Y. Ge, W. T. Meng, G. X. Liu, S. L. Liu, S. C. Mu, Cation/Anion Dual-Vacancy Pair Modulated Atomically-Thin Se_x-Co_3S_4 Nanosheets with Extremely High Water Oxidation Performance in Ultralow-Concentration Alkaline Solutions, *Small* 2022, **18**, 2108097.

[46] M. Wang, Y. Q. Wang, S. S. Mao, S. H. Shen, Transition-metal alloy electrocatalysts with active sites modulated by metal-carbide heterophases for efficient oxygen evolution, *Nano Energy* **2021**, *88*, 106216.

[47] D. H. Duan, D. S. Guo, J. Gao, S. B. Liu, Y. F. Wang, Electrodeposition of cobalt-iron bimetal phosphide on Ni foam as a bifunctional electrocatalyst for efficient overall water splitting, *J. Colloid Interf. Sci.* 2022, **622**, 250–260.

[48] J. X. Chen, Q. W. Long, K. Xiao, T. Ouyang, N. Li, S. Y. Ye, Z.-Q. Liu, Vertically-interlaced NiFeP/MXene electrocatalyst with tunable electronic structure for high-efficiency oxygen evolution reaction, *Sci. Bull.* **2021**, *66*, 1063–1072.

[49] X. G. Li, J. H. Zhou, C. Liu, L. Xu, C. L. Lu, J. Yang, H. Pang, W. H. Hou, Encapsulation of Janus-structured Ni/Ni_2P nanoparticles within hierarchical wrinkled N-doped carbon nanofibers: Interface engineering induces high-efficiency water oxidation, *Appl. Catal. B.* 2021, **298**, 120578.

[50] Y. Huang, S. L. Zhang, X. F. Lu, Z. P. Wu, D. Y. Luan, X. W. Lou, Trimetallic Spinel $NiCo_{2-x}Fe_xO_4$ Nanoboxes for Highly Efficient Electrocatalytic Oxygen Evolution, *Angew. Chem. Int. Ed.* 2021, **60**, 11841–11846.

[51] T. I. Singh, G. Rajeshkhanna, U. N. Pan, T. Kshetri, H. Lin, N. H. Kim, J. H. Lee, Alkaline Water Splitting Enhancement by MOF-Derived Fe-Co-Oxide/Co@NC-mNS Heterostructure: Boosting OER and HER through Defect Engineering and In Situ Oxidation, *Small* 2021, **17**, 2101312.

[52] W. M. Li, S. H. Chen, M. X. Zhong, C. Wang, X. F. Lu, Synergistic coupling of NiFe layered double hydroxides with Co-C nanofibers for high-efficiency oxygen evolution reaction, *Chem. Eng. J.* 2021, **415**, 128879.